AGU PUBLICATIONS

JGR

Journal of Geophysical Research: Space Physics

RESEARCH ARTICLE
10.1002/2015JA022278

**Key Points:**
- The delay times of $L_{pp}$ to the arrival of $L_{pp}$ indicators is a function of MLT
- The MLT dependence of plasmapause formation is in agreement with the mechanism of interchange instability
- At high geomagnetic activity the $L_{pp}$ bulge is formed in the postdusk; at low geomagnetic activity the bulge is located close to midnight

**Correspondence to:**
G. Verbanac,
giuli1.verbanac@gmail.com

**Citation:**
Bandić, M., G. Verbanac, M. B. Moldwin, V. Pierrard, and G. Piredda (2016), MLT dependence in the relationship between plasmapause, solar wind, and geomagnetic activity based on CRRES: 1990–1991, *J. Geophys. Res. Space Physics*, *121*, 4397–4408, doi:10.1002/2015JA022278.

Received 23 NOV 2015
Accepted 15 APR 2016
Accepted article online 2 MAY 2016
Published online 21 MAY 2016
Corrected 7 JUN 2016

This article was corrected on 7 JUN 2016. See the end of the full text for details.



# MLT dependence in the relationship between plasmapause, solar wind, and geomagnetic activity based on CRRES: 1990–1991

**Mario Bandić[1], Giuli Verbanac[2], Mark B. Moldwin[3], Viviane Pierrard[4,5], and Giovanni Piredda[6]**

[1]Munich, Germany, [2]Department of Geophysics, University of Zagreb, Zagreb, Croatia, [3]Climate and Space Sciences and Engineering, University of Michigan, Ann Arbor, Michigan, USA, [4]Royal Belgian Institute for Space Aeronomy (Space Physics and STCE), Brussels, Belgium, [5]Earth and Life Institute, TECLIM, Université Catholique de Louvain, Belgium, [6]Research Centre for Microtechnology, University of Applied Sciences, Dornbirn, Austria

**Abstract** Using the database of CRRES in situ observations of the plasmapause crossings, we develop linear and more complex plasmapause models parametrized by (a) solar wind parameters *V* (solar wind velocity), *BV* (where *B* is the magnitude of the interplanetary magnetic field (IMF)), and $d\Phi_{mp}/dt$ (which combines different physical mechanisms which run magnetospheric activity), and (b) geomagnetic indices *Dst*, *Ap*, and *AE*. The complex models are built by including a first harmonic in magnetic local time (MLT). Our method based on the cross-correlation analyses provides not only the plasmapause shape for different levels of geomagnetic activity but additionally yields the information of the delays in the MLT response of the plasmapause. All models based on both solar wind parameters and geomagnetic indices indicate the maximal plasmapause extension in the postdusk side at high geomagnetic activity. The decrease in the convection electric field places the bulge toward midnight. These results are compared and discussed in regard to past works. Our study shows that the time delays in the plasmapause response are a function of MLT and suggests that the plasmapause is formed by the mechanism of interchange instability motion. We observed that any change quickly propagates across dawn to noon, and then at lower rate toward midnight. The results further indicate that the instability may propagate much faster during solar maximum than around solar minimum. This study contributes to the determination of the MLT dependence of the plasmapause and to constrain physical mechanism by which the plasmapause is formed.

## 1. Introduction

The plasmasphere is an area in the inner magnetosphere which contains trapped, low-energy, and dense plasma. The plasmapause is the outer boundary of the plasmasphere whose dynamics are determined by a combination of the two electric fields: corotation and convection electric fields [e.g., *Nishida*, 1966; *Lemaire and Gringauz*, 1998].

Since plasmapause influences the ring current dynamic [e.g., *Kozyra et al.*, 1995], radiation belts [e.g., *Horne and Thorne*, 1998; *Lorentzen et al.*, 2001; *Darrouzet et al.*, 2013], and formation and propagation of electromagnetic waves [e.g., *Takahashi and Anderson*, 1992], it is important to know its time-dependent location.

The plasmapause positions ($L_{pp}$) have been estimated both theoretically and empirically. The $L_{pp}$ dynamics are studied theoretically by considering (i) the last closed equipotential of the convection electric field [*Brice*, 1967; *Lemaire and Pierrard*, 2008] and (ii) the peeling of the plasmasphere [*Lemaire and Gringauz*, 1998; *Pierrard and Lemaire*, 2004; *Lemaire and Pierrard*, 2008]. This second process implicates a magnetic local time (MLT) dependence of the plasmapause position that can be verified empirically. Empirically, $L_{pp}$ has been evaluated by studying the following: ground-based whistler data; in situ satellite observations of plasma density (e.g., ISEE and CRRES), electron plasma frequency (Cluster), and thermal velocity (THEMIS); field-aligned current observations (CHAMP), as a function of geomagnetic indices [e.g., *O'Brien and Moldwin*, 2003; *Liu et al.*, 2015; *Verbanac et al.*, 2015, and reference therein]; and solar wind parameters [*Larsen et al.*, 2007; *Cho et al.*, 2015; *Verbanac et al.*, 2015]. All these studies have shown that the plasmapause shrinks when geomagnetic activity increases achieving the largest extension in the dusk side.

Most of the previous empirical studies used the maximum (or minimum) in the geomagnetic indices or in the solar wind (thereafter SW) parameters during hours to days prior to the plasmapause crossing. For instance, *Carpenter and Anderson* [1992] established linear relationship between $L_{PP}$ and the maximum of geomagnetic *Kp* index observed in the previous 24 h relative to the plasmapause crossing. *Moldwin et al.* [2002] linked the $L_{PP}$ with the maximum *Kp* index found in the previous 12 h separately for night, dawn, day, and dusk sectors. *O'Brien and Moldwin* [2003] obtained linear relationships between $L_{PP}$ and maximum *Kp* index taken from 36 to 2 h relative to the plasmapause crossing, maximum *AE* index, and minimum *Dst* index taken in the previous 36 h and 24 h, respectively. They also fitted a function to the observed $L_{PP}$ values that depends both on geomagnetic indices and MLT. Following this work, *Liu and Liu* [2014] obtained plasmapause model based on THEMIS measurements. Similarly, *Heilig and Lühr* [2013] expressed $L_{PP}$ based on field-aligned currents as a function of *Kp*, $Kp^2$, and MLT. *Cho et al.* [2015] presented the models averaged in MLTs, based on THEMIS plasmapause crossings and extrema (minimum or maximum) of some solar wind variables (e.g., velocity *V*, *z* component of the IMF vector $B_z$, Akasofu's epsilon parameter, *y* component of the solar wind electric field *E*, and IMF clock angle $\theta$) and geomagnetic indices *Kp*, *Dst*, and *AE*, all taken within the selected time windows. *Liu et al.* [2015] obtained multi-index plasmapause model also using THEMIS measurements and geomagnetic indices: mean *AE*, mean *Kp*, mean *AL*, maximum *AU*, and maximum *SYM-H* taken within the determined time window for each input parameter and for each MLT sector.

*Larsen et al.* [2007] provide the delay in the response of plasmapause averaged in MLT to the arrival of $B_z$, $\theta$, and polar cap potential drop $\phi$. *Verbanac et al.* [2015] obtained $L_{PP}$ fits for three different MLT sectors (night, day, and evening) based on solar wind coupling functions ($B_z$, *BV*, and $d\Phi_{mp}/dt$ defined in section 2) and geomagnetic indices (*Ap*, *Dst*, and *AE*). They showed that different regions of the plasmapause react with different delay times to the arrival of the investigated $L_{PP}$ indicators which are function of MLT.

In the present study, we apply the approach presented in *Verbanac et al.* [2015] (hereafter Paper I) to the CRESS-based $L_{PP}$ database developed by *Moldwin et al.* [2002] (hereafter Paper II) that contains about 3 times more data than analyzed in Paper I and during a more geomagnetically active period.

Worth noting is that the MLT dependence of the time lags in the response of plasmapause obtained with our method is very valuable information which can help in constraining the physical mechanism by which the plasmapause is formed.

The main aims are (i) to investigate the MLT dependence in the relationship between CRRES-based plasmapause, solar wind, and geomagnetic activity; (ii) to compare the obtained plasmapause shapes with those derived from different models; (iii) to investigate the response of the plasmapause to $L_{PP}$ indicators during different phases of the solar activity cycle; and (iv) try to constrain physical mechanism by which the plasmapause is formed.

We build simple empirical $L_{PP}$ models using solar wind parameters *V*, *BV*, $d\Phi_{mp}/dt$, and geomagnetic indices *Ap*, *Dst*, and *AE* as indicators of the $L_{PP}$ for different MLT sector divisions and investigate the dependence of the obtained delay times on MLTs. We further develop more complex models by including a first harmonic in MLT. The results are compared with those obtained by other studies in order to discuss the plasmapause shape from different models. Further comparison of the obtained time delays with those based on Cluster plasmapause as presented in Paper I is performed to investigate the plasmapause responses during different phases of solar activity cycle.

The paper is organized as follows. Data and method of analyses are presented in section 2. Section 3 contains the results of the obtained best linear fits and of the continuous MLT models. Comparison with results from other studies is given in section 4. Discussion is given in section 5, and conclusions are drawn in the last section.

## 2. Data and Method

To study the $L_{PP}$, we used following data: 1 h averages of geomagnetic indices *Dst* and *AE*; 3 h averages of the geomagnetic index *Ap*; 1 h averages of the solar wind velocity *V*, IMF magnitude *B*, and components $B_x$, $B_y$, and $B_z$ in GSM (geocentric solar magnetospheric) of the IMF vector **B**; and data set of plasmapause positions based on the plasma wave receiver that was on board CRRES satellite.

Within the studied period there are a lot of gaps in the solar wind data, which are often long lasting (5–8 days). Roughly 55% of solar wind data are missing.

**Table 1.** Number of $L_{pp}$ (in Three- and Four-Sector Divisions and for All MLTs) for Investigated $L_{pp}$ Indicators[a]

| | *V* | *BV* | $d\Phi_{mp}/dt$ | GI |
|---|---|---|---|---|
| Sect1 (MLT 01–07) | 121 | 115 | 115 | 364 |
| Sect2 (MLT 07–16) | 85 | 84 | 84 | 249 |
| Sect3 (MLT 16–01) | 94 | 89 | 89 | 350 |
| SectI (MLT 00–06) | 129 | 123 | 123 | 393 |
| SectII (MLT 06–12) | 78 | 76 | 76 | 226 |
| SectIII (MLT 12–18) | 25 | 24 | 24 | 102 |
| SectIV (MLT 18–24) | 68 | 65 | 65 | 242 |
| All | 300 | 288 | 288 | 963 |

[a]GI represents geomagnetic indices (GI = *Dst*, *Ap*, *AE*).

We used the data set of 963 plasmapause positions obtained from in situ CRRES electron density observations made in 1990–1991. For the description of the methodology employed to identify the $L_{PP}$ we refer to Paper II. There is a gap in the data coverage around noon at larger radial distances and near midnight at middle radial distance. Also, because of the orbital characteristics plasmapause at L shell >7 could not be collected.

We employed the following solar wind-based $L_{PP}$ indicators: *V*, *BV*, and $d\Phi_{mp}/dt$ [*Newell et al.*, 2007] defined as:

$$\Phi_{mp}/dt = V^{4/3}B_T^{2/3}\sin^{8/3}(\theta_c/2) \quad (1)$$

where $B_T = \sqrt{B_y^2 + B_z^2}$ and $\theta_c = \arctan(B_y/B_z)$.

For these solar wind parameters we were able to obtain stable cross-correlation results. The importance of solar wind coupling functions *BV* and $d\Phi_{mp}/dt$ in accounting for much about the magnetospheric activity is explained in our previous work (Paper I). Here we only shortly discuss their physical meaning. $B_z$ is related to the reconnection of the IMF with the Earth's magnetic field, the process that is important for strengthening the magnetospheric convection. *BV* is proportional to the interplanetary electric field. $d\Phi_{mp}/dt$ takes into account different physical processes related to the magnetospheric activity. In addition to the previously mentioned solar wind parameters, past work has shown that the plasmapause location is well correlated with *V* [*Cho et al.*, 2015]. Furthermore, *Verbanac et al.* [2011, 2013] have reported a strong relationship between geomagnetic indices and *V* during both solar minimum and solar maximum. We therefore also test the plasmapause response to this solar wind parameter in this study.

The relationships between the $L_{PP}$ and $L_{PP}$ indicators are investigated binning the data in three and four MLT sectors as follows: (three sectors) Sector1 (01–07 MLT), Sector2 (07–16 MLT), and Sector3 (16–01 MLT); (four "traditional" sectors): SectorI (00–06 MLT), SectorII (06–12 MLT), SectorIII (12–18 MLT), SectorIV (18–00 MLT), and also when all MLTs are taken together.

The MLT intervals in both three- and four-sector divisions were carefully chosen to provide reliable statistics in each time bin. The three-sector division is the same as in Paper I, allowing us to directly compare the obtained results with our previous work.

Employing the cross-correlation analysis, we obtain the time lags of the plasmapause response to $L_{PP}$ indicators and linear least squares fit parameters for the highest-correlation time lags which describe the relationship between the $L_{PP}$ and different $L_{PP}$ indicators. Following our previous study (Paper I), we consider here the time window of 30 h before the plasmapause crossings. For detailed description of the employed cross-correlation analysis, the reader is referred to Paper I.

Concerning solar wind-based $L_{PP}$ indicators, the cross-correlation analyses are performed only if there were ≥70% data in the interval of 30 h preceding the UT of each of the plasmapause crossing. Imposing this criterion, we analyze ~300 $L_{PP}$, similar to the number of $L_{PP}$ investigated in Paper I, which is adequate to perform reliable statistics. The number of plasmapause positions meeting this condition for each of the solar wind $L_{pp}$ indicator in both three- and four-sector divisions is given in Table 1. For geomagnetic indices (thereafter *GI*), all the available $L_{pp}$ in each sector are used (in total 963 $L_{pp}$), and the numbers are also displayed in Table 1. Note that in four-sector division, SectorIII (12–18 MLT) contains significantly less data than other sectors. For solar wind-based $L_{PP}$ indicators, the numbers of $L_{pp}$ are additionally reduced due to the gaps in solar wind data. Thus, for solar wind parameters we focus on the three-sector division only in order to ensure reliable statistics.

**Table 2.** Time Lags $\Delta t$ (in Hours) of the Relationship Between $L_{PP}$ and $L_{PP}$ Indicators (*Dst*, *Ap*, *AE*, *V*, *BV*, and $d\Phi_{mp}/dt$) for the Highest-Correlation Time Lags Obtained With Cross-Correlation Analyses[a]

| | $\Delta t_1$ | $\Delta t_2$ | $\Delta t_3$ | $\Delta t_{all}$ | $\sigma_1$ | $\sigma_2$ | $\sigma_3$ | $\sigma_{all}$ | $R_{all}$ |
|---|---|---|---|---|---|---|---|---|---|
| *Dst*-$L_{pp}$ | 1 | 3 | 10 | 3 | 0.75 | 0.61 | 0.92 | 0.83 | 0.54 |
| *Ap*-$L_{pp}$ | 3 | 8 | 19 | 3 | 0.81 | 0.72 | 0.96 | 0.90 | −0.39 |
| *AE*-$L_{pp}$ | 1 | 9 | 20 | 4 | 0.76 | 0.68 | 0.92 | 0.86 | −0.49 |
| *V*-$L_{pp}$ | 4 | 3 | 7 | 4 | 0.75 | 0.61 | 0.87 | 0.79 | −0.49 |
| *BV*-$L_{pp}$ | 4 | 12 | 18 | 4 | 0.76 | 0.71 | 0.90 | 0.85 | −0.40 |
| $d\Phi_{mp}/dt$-$L_{pp}$ | 6 | 9 | 18 | 11 | 0.79 | 0.73 | 0.85 | 0.86 | −0.41 |

[a] $\sigma$ values are the RMS errors of the best $L_{PP}$ fits. Subscripts *i* and all refer to the MLT Sector1–Sector3 (01–07 MLT, 07–16 MLT, and 16–01 MLT) and to all MLTs sectors, respectively. The last column contains the correlation coefficients (*R*) obtained when all MLTs are taken together.

## 3. Results

### 3.1. Best Linear Fit Models

Here we present the results obtained employing the cross-correlation analysis, as explained in the previous section. In Table 2 we present the time lags $\Delta t$, and the RMS errors (RMSEs) of the best fits obtained by binning the data into three MLT sectors (01–07 MLT, 07–16 MLT, and 16–01 MLT) as well as for all MLTs taken together. The correlation coefficients are given for the case when all MLTs are taken together. For GI we additionally show $\Delta t$ and RMSE of the best fits for four MLT sector divisions (00–06 MLT, 06–12 MLT, 12–18 MLT, 18–00 MLT) in Table 3.

The RMS errors displayed in both tables are approximately 0.6–1 L in all MLTs taken together or in sectors. The sectors that comprise dusk and evening (Sector3 in the three-sector division and SectorIV in the four-sector division) have considerably more scatter than the other MLT sectors. The lowest model RMSEs found in Sector2 for three-sector divisions and in SectorIII for four-sector divisions likely reflect the absence of $L_{PP} > 5$ on the dayside and generally less plasmapause data between 12 MLT and 18 MLT (for the details about the data coverage the reader is referred to Paper II). We calculate the statistical significance of the RMSE differences between models using a Monte Carlo bootstrap procedure. We first generate distributions of RMSEs for each model by creating the data samples from the original data set using random selection with replacement. For each pair of the RMSE distributions within each column of Tables 2 and 3, we then calculate the probability to observe a larger RMSE in the first distribution belonging to the pair than in the second. If this probability is larger than 0.95 or smaller than 0.05, then the two RMSEs are considered to be distinguishable. These calculations provide following results. For three-sector division, only *Dst* in the day sector (07–16 MLT) provides a relatively superior model since it is the only model which is statistically distinguishable from *Ap* model even if not from all other $L_{PP}$ models. The RMSEs of all other models are not statistically distinguishable from the RMSEs of any model. Note that although *V* in Sector2 (07–16 MLT) has the same RMSE as *Dst*, and lower than other $L_{PP}$ indicators, the probability of observing larger RMSE than any of the others, taken individually, is of the order of 10%. For four-sector division *Dst* is statistically distinguishable from both *Ap* and *AE* in SectorII (06–12 MLT) and provides the best model in this sector. Note that *AE* in SectorIII (12–18 MLT) has the lowest RMSE, but there is no statistical significance of the differences in regard to *Dst* and *Ap* models. Our calculations give 25% probability of observing a higher value of *AE* RMSE than the RMSE observed for the other two models.

**Table 3.** Time Lags $\Delta t$ (in Hours) of the Relationship Between $L_{PP}$ and $L_{PP}$ Indicators (*Dst*, *Ap*, and *AE*) for the Highest-Correlation Time Lags Obtained With Cross-Correlation Analyses[a]

| | $\Delta t_I$ | $\Delta t_{II}$ | $\Delta t_{III}$ | $\Delta t_{IV}$ | $\sigma_I$ | $\sigma_{II}$ | $\sigma_{III}$ | $\sigma_{IV}$ |
|---|---|---|---|---|---|---|---|---|
| *Dst*-$L_{pp}$ | 1 | 2 | 7 | 10 | 0.74 | 0.60 | 0.72 | 0.97 |
| *Ap*-$L_{pp}$ | 3 | 5 | 19 | 28 | 0.79 | 0.74 | 0.73 | 1.02 |
| *AE*-$L_{pp}$ | 1 | 4 | 19 | 29 | 0.75 | 0.70 | 0.67 | 0.96 |

[a] The last four columns are the RMS errors ($\sigma$) of the best $L_{PP}$ fits. Subscripts *i* refer to the MLT Sectors I-IV (00–06 MLT, 06–12 MLT, 12–18 MLT, 18–00 MLT), respectively.

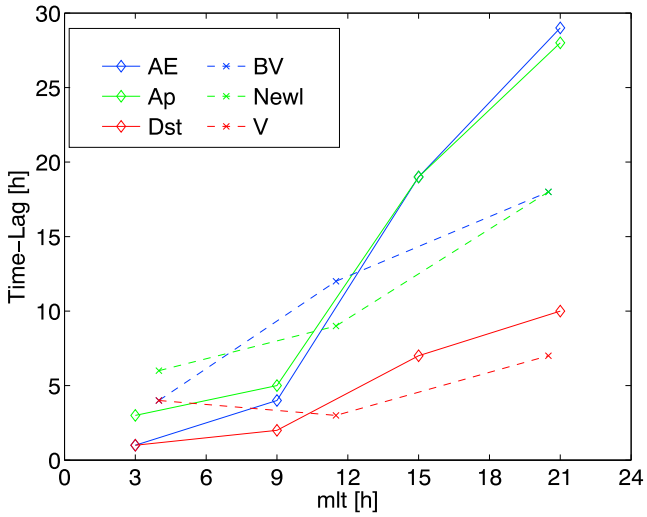


**Figure 1.** Time lag versus MLT obtained by binning the data into 6 h MLT for geomagnetic indices (solid lines) and into three MLT sectors for solar wind-based $L_{PP}$ indicators (dashed lines).

The main conclusion that comes out of Tables 2 and 3 is that for all $L_{PP}$ indicators, the time lag corresponding to the highest correlation is a function of MLT. The obtained time lags ascend from Sector1 to Sector3/SectorIV. The only exception is parameter *V*, where the lags in Sector1 and Sector2 are comparable. Similar $\Delta t$ values are obtained for *Ap* and *AE*, and notably shorter $\Delta t$ for *Dst* and *V* (2–12 h shorter depending on the sector). Intermediate lags are found for both *BV* and $d\Phi_{mp}/dt - L_{pp}$. Time lag versus MLT is shown in Figure 1. The plotted lags are obtained by binning the data into 6 h MLT for GI, and into three MLT sectors for solar wind-based $L_{PP}$ indicators. We note here that the observed MLT dependence of the time lags indicates that the plasmapause is first formed in the postmidnight to dawnside, and later in other MLTs. The more detailed discussion is given in sections 4 and 6.

The coefficients of the best linear fit models are given in Table 4. We present the fit coefficients for three-sector division in order to analyze them for all $L_{PP}$ indicators. Recall that for solar wind-based $L_{PP}$ indicators, data could not be adequately described if binned into four MLT sectors, due to the lower number of $L_{PP}$ between 12 MLT and 18 MLT and due to additional gaps in the solar wind data.

The shape of the plasmapause was examined in respect to low and high values of $L_{PP}$ indicators as identified from the analyzed data sets. However, note that the developed models work for any given geomagnetic index or solar wind parameters thus not only for some extreme values (low and high values). In Table 5 the fitted $L_{PP}$ values for low and high geomagnetic activity are shown. Based on all $L_{PP}$ relationships, the lowest $L_{PP}$ is found in Sector2 and amounts to ~2.8 $R_E$. We link this $L_{PP}$ value to the indicator values at high geomagnetic activity.

**Table 4.** Linear Least Squares Fits ($y = ax + b$) for the Relationships Between $L_{PP}$ and $L_{PP}$ Indicators (*V*, *BV*, $d\Phi_{mp}/dt$, *Dst*, *Ap*, and *AE*) for the Highest-Correlation Time Lags[a]

| | $a_1$ | $b_1$ | $a_2$ | $b_2$ | $a_3$ | $b_3$ | $a_{all}$ | $b_{all}$ |
|---|---|---|---|---|---|---|---|---|
| *Dst* | $(2.00 \pm 0.15) \times 10^{-2}$ | $4.53 \pm 0.05$ | $(2.03 \pm 0.15) \times 10^{-2}$ | $4.08 \pm 0.06$ | $(1.53 \pm 0.16) \times 10^{-2}$ | $4.56 \pm 0.06$ | $(1.93 \pm 0.10) \times 10^{-2}$ | $4.45 \pm 0.03$ |
| *Ap* | $(-2.30 \pm 0.22) \times 10^{-2}$ | $4.56 \pm 0.05$ | $(-1.45 \pm 0.18) \times 10^{-2}$ | $3.83 \pm 0.06$ | $(-1.52 \pm 0.21) \times 10^{-2}$ | $4.49 \pm 0.06$ | $(-1.65 \pm 0.12) \times 10^{-2}$ | $4.34 \pm 0.04$ |
| *AE* | $(-2.48 \pm 0.19) \times 10^{-3}$ | $4.74 \pm 0.06$ | $(-1.73 \pm 0.17) \times 10^{-3}$ | $4.06 \pm 0.07$ | $(-1.91 \pm 0.21) \times 10^{-3}$ | $4.71 \pm 0.07$ | $(-2.04 \pm 0.12) \times 10^{-3}$ | $4.57 \pm 0.04$ |
| *V* | $(-6.80 \pm 1.11) \times 10^{-3}$ | $7.16 \pm 0.48$ | $(-6.00 \pm 0.92) \times 10^{-3}$ | $6.41 \pm 0.43$ | $(-4.81 \pm 1.19) \times 10^{-3}$ | $6.24 \pm 0.51$ | $(-5.75 \pm 0.65) \times 10^{-3}$ | $6.54 \pm 0.29$ |
| *BV* | $(-3.18 \pm 0.60) \times 10^{-1}$ | $5.27 \pm 0.20$ | $(-2.04 \pm 0.45) \times 10^{-1}$ | $4.44 \pm 0.18$ | $(-1.66 \pm 0.66) \times 10^{-1}$ | $4.80 \pm 0.26$ | $(-2.22 \pm 0.32) \times 10^{-1}$ | $4.87 \pm 0.13$ |
| $d\Phi_{mp}/dt$ | $(-1.39 \pm 0.28) \times 10^{-4}$ | $4.83 \pm 0.13$ | $(-1.02 \pm 0.23) \times 10^{-4}$ | $4.11 \pm 0.13$ | $(-1.13 \pm 0.29) \times 10^{-4}$ | $4.70 \pm 0.16$ | $(-0.92 \pm 0.13) \times 10^{-4}$ | $4.52 \pm 0.08$ |

[a]Subscripts *i* and all refer to the MLT Sector1 – Sector3 and to all MLTs sectors, respectively.

**Table 5.** The $L_{PP}$ Obtained From the Linear Least Square Fits for Two Values of Each of the $L_{PP}$ Indicator[a]

| | *V* (km s$^{-1}$) | | *BV* (mV m$^{-1}$) | | $d\Phi_{mp}/dt$ (km s$^{-1}$)$^{4/3}$ (nT)$^{2/3}$ | | *Dst* (nT) | | *Ap* (nT) | | *AE* (nT) | |
|---|---|---|---|---|---|---|---|---|---|---|---|---|
| | 340 | 580 | 2 | 7.5 | $0.1 \times 10^4$ | $1.35 \times 10^4$ | 10 | −60 | 5 | 65 | 30 | 650 |
| Sect1 | 4.85 | 3.22 | 4.63 | 2.89 | 4.69 | 2.96 | 4.73 | 3.33 | 4.44 | 3.06 | 4.66 | 3.13 |
| Sect2 | 4.37 | 2.93 | 4.03 | 2.91 | 4.01 | 2.74 | 4.29 | 2.86 | 3.76 | 2.89 | 4.00 | 2.93 |
| Sect3 | 4.61 | 3.45 | 4.46 | 3.55 | 4.59 | 3.18 | 4.72 | 3.65 | 4.41 | 3.50 | 4.65 | 3.47 |
| SecAll | 4.58 | 3.20 | 4.43 | 3.20 | 4.42 | 3.28 | 4.64 | 3.29 | 4.26 | 3.27 | 4.51 | 3.25 |

[a]The first one is related to the low indicator values, the second one to that at which $L_{PP}$ amounts to ~2.8 $R_E$.

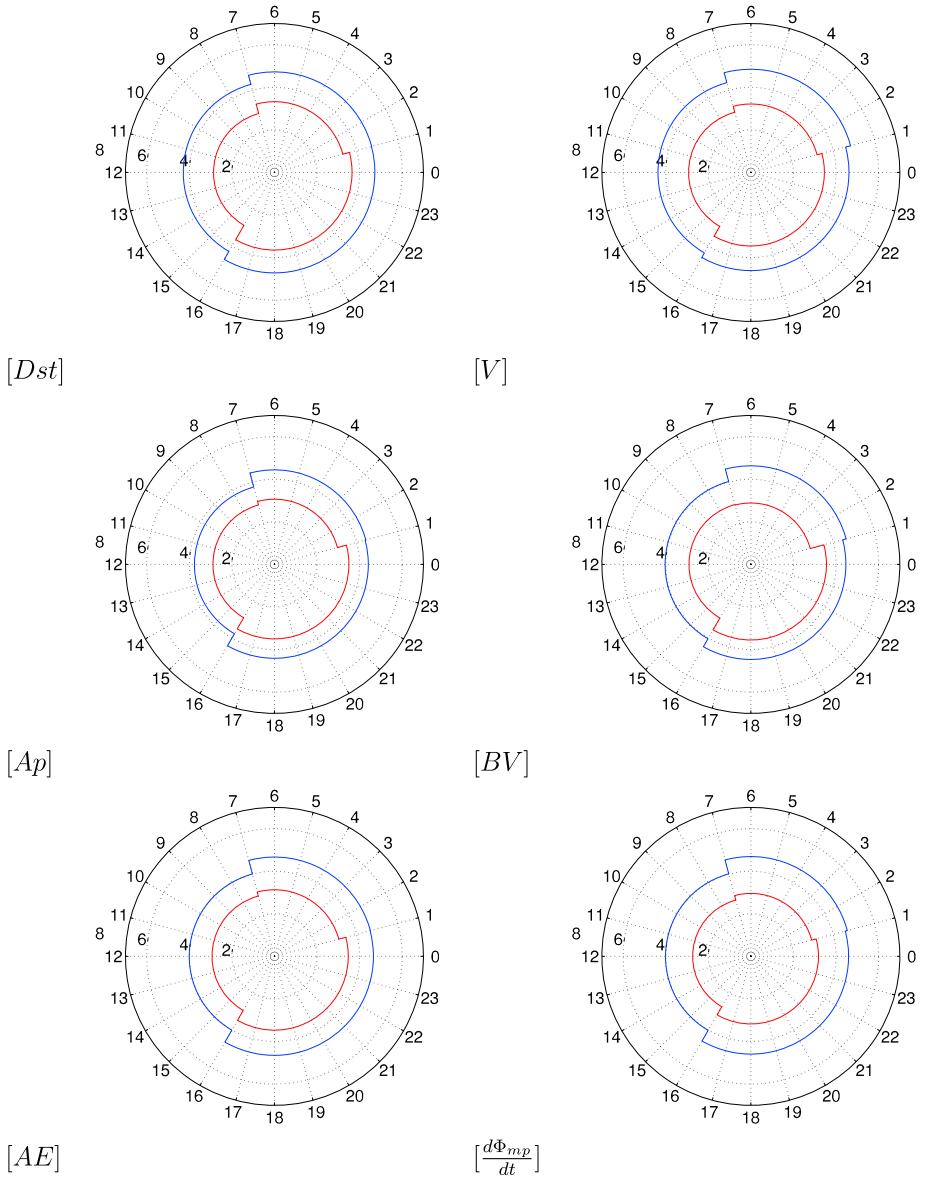


**Figure 2.** The $L_{pp}$ in three MLT sectors from linear fit models based on the following: (left column) *Dst*, *Ap*, and *AE* and (right column) *V*, *BV*, and $d\Phi_{mp}/dt$. Blue and red lines indicate low and high geomagnetic activity as given in Table 5, respectively.

**Table 6.** The Parameters of the Best Fit Complex Models for the Highest-Correlation Time Lag and RMSE

| | Fit | | | | | | RMSE | | | | |
|---|---|---|---|---|---|---|---|---|---|---|---|
| | $a_1 \times 10^2$ | $a_{mlt} \times 10^1$ | $(24/2\pi)a_\phi$ | $b_1$ | $b_{mlt} \times 10^1$ | $(24/2\pi)b_\phi$ | $\sigma_1$ | $\sigma_2$ | $\sigma_3$ | $\sigma_4$ | $\sigma_{all}$ |
| *Dst* | $1.91 \pm 0.10$ | $2.83 \pm 0.77$ | $7.57 \pm 1.27$ | $4.42 \pm 0.04$ | $0.64 \pm 0.13$ | $23.38 \pm 0.87$ | 0.75 | 0.58 | 0.73 | 0.95 | 0.77 |
| *Ap* | $-2.07 \pm 0.14$ | $-1.61 \pm 0.92$ | $18.85 \pm 3.34$ | $4.37 \pm 0.04$ | $0.79 \pm 0.15$ | $23.16 \pm 0.72$ | 0.81 | 0.71 | 0.76 | 1.00 | 0.83 |
| *AE* | $-0.22 \pm 0.01$ | $-1.34 \pm 0.72$ | $13.62 \pm 2.85$ | $4.57 \pm 0.04$ | $0.82 \pm 0.14$ | $22.58 \pm 0.73$ | 0.76 | 0.68 | 0.70 | 0.95 | 0.79 |

The $L_{pp}$ values reported in Table 5 together with the RMSE given in Table 2 indicate that at quiet time the bulge is likely located in the premidnight side as concerning GI. The given solar wind-based plasmapause values are indistinguishable in Sector1 and Sector3 within the error limits. At higher activity the bulge is located in Sector3 according to all $L_{pp}$ indicators.

Figure 2 shows the location of the plasmapause for each model for two identified levels of geomagnetic activity as given in Table 5.

### 3.2. Continuous MLT Models

We further develop more complex models by including a first harmonic in MLT. For a certain $L_{pp}$ indicator $Q$ at a given MLT, plasmapause position is expressed as

$$L_{pp} = AA \cdot Q + BB \tag{2}$$

*AA* and *BB* are defined as

$$AA(\phi) = a_1 \left[1 + a_{mlt} \cos(\phi - a_\phi)\right]; BB(\phi) = b_1 \left[1 + b_{mlt} \cos(\phi - b_\phi)\right]$$

where $\phi = 2\pi(\mathrm{MLT}/24)$.

To determine the set of model coefficients ($a_1$, $a_{mlt}$, $a_\phi$, $b_1$, $b_{mlt}$, and $b_\phi$), first, some finite MLT division has to be chosen. A linear regression in each sector is then performed ($L_{pp} = aQ + b$), and pairs of coefficients $a$ and $b$ are obtained, by which the model coefficients are calculated. As initial MLT bins, we selected four MLT sector division to maximize as much as possible the resolution in MLT and also to enable enough data in each sector for adequate statistics. This unfortunately allows us only to build models using geomagnetic indices. Recall that for solar wind-based $L_{pp}$ indicators, only binning the data into three MLT sectors was possible. The parameters of the obtained MLT plasmapause model are given in Table 6. The errors of the parameters are calculated with a Monte Carlo approach. We generate samples of the distribution of the linear regression coefficients ($a$ and $b$) assuming that they are independent and distributed with Gaussian probability. For each sample we then calculate the model coefficients in order to obtain their probability distribution from which we determine their standard deviations. In this way we did not have to assume that the errors are small, as required by, e.g., error propagation formulae.

The RMSEs reported in Table 6 are very similar to those for simpler models given in Table 3. Only when all local times are considered, the RMSE are reduced compared to simpler models.

We note that following coefficients and their products, $a_\phi$, $b_\phi$, $a_1Q + b_1$, $a_1 a_{mlt} Q$, and $b_1 b_{mlt}$, determine the plasmapause shape. The location of the bulge is given by the phase containing the combination of these coefficient products, and not with $a_\phi$, $b_\phi$ solely as argued in *O'Brien and Moldwin* [2003].

Figure 3 (right column) depicts $L_{pp}$(MLT) for each model and for two levels of geomagnetic activity, as given in Table 5. Blue and red lines indicate low activity and high activity, respectively. The symbols show the MLT of maximum $L_{pp}$ for each continuous model. To compare with the simpler models obtained from the cross-correlation analysis, we also show the $L_{pp}$ in four MLT bins (Figure 3, left column). Simple *Ap* and *Dst* models for low activity cannot resolve whether the maximum plasmapause extension is in SectorI or in SectorIV, while simple *AE* model indicates the bulge location in SectorIV. Continuous MLT models give a maximum $L_{pp}$ between 22 MLT and 0 MLT, depending on the model. At high activity the bulge is observed in SectorIV, according to all of simple models. Continuous models provide the maximum $L_{pp}$ at around 21 MLT. All these indicate the midnight/premidnight plasmapause bulge which rotates toward dusk as geomagnetic activity increases.

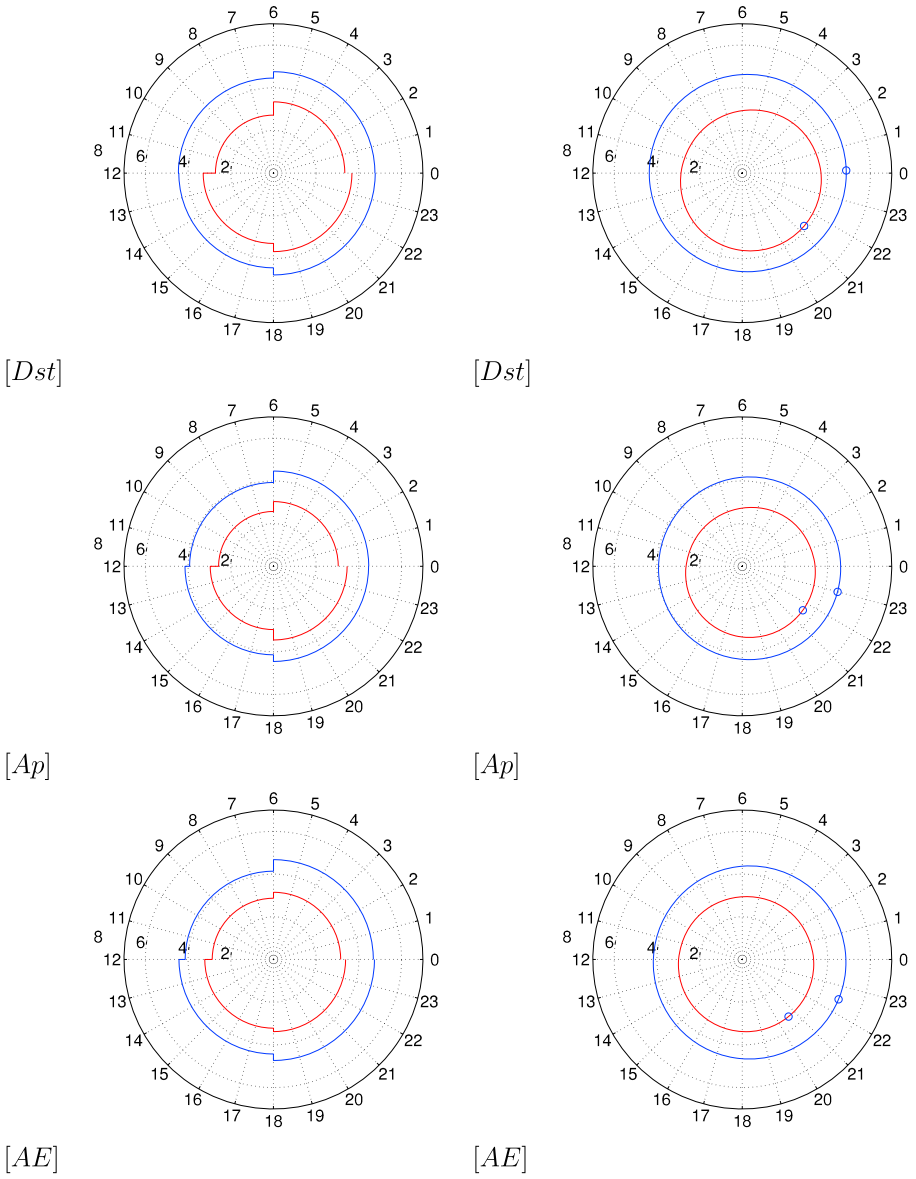


**Figure 3.** The $L_{pp}$ from (left column) linear fit models in four MLT sectors and (right column) continuous MLT models. Blue and red lines indicate low and high geomagnetic activity. The symbols indicate the MLT of maximum $L_{pp}$ for each continuous model as given in Table 5, respectively.

## 4. Comparison With Past Studies

In the following we first compare the plasmapause shapes from our models (denoted as CRRES2 models) with those presented by *O'Brien and Moldwin* [2003], *Liu and Liu* [2014], and *Liu et al.* [2015] (denoted as CRRES1, THEMIS1, and THEMIS2 models, respectively).

We could compare only our models that are based on geomagnetic indices with others, since none of these previous models are based on solar wind parameters. The past studies utilize the procedure of identifying the time window with respect to the plasmapause crossing over which the maximum (or minimum) or/and mean of the $L_{pp}$ indicator is then determined. This approach is widely used for plasmapause modeling [e.g., *Carpenter and Anderson*, 1992; *Moldwin et al.*, 2002; *Cho et al.*, 2015]. On the other side, our method employs the $L_{pp}$ indicator values at the highest-correlation time lags and additionally provides the delays in the MLT response of the plasmapause. For comparison, plasmapause is simulated for two levels of geomagnetic activity (low and high) using each of these models. For CRRES1, THEMIS1, and CRRES2 the comparison is performed for both *AE*- and *Dst*-based models. When calculating predictions from CRRES1 and THEMIS1

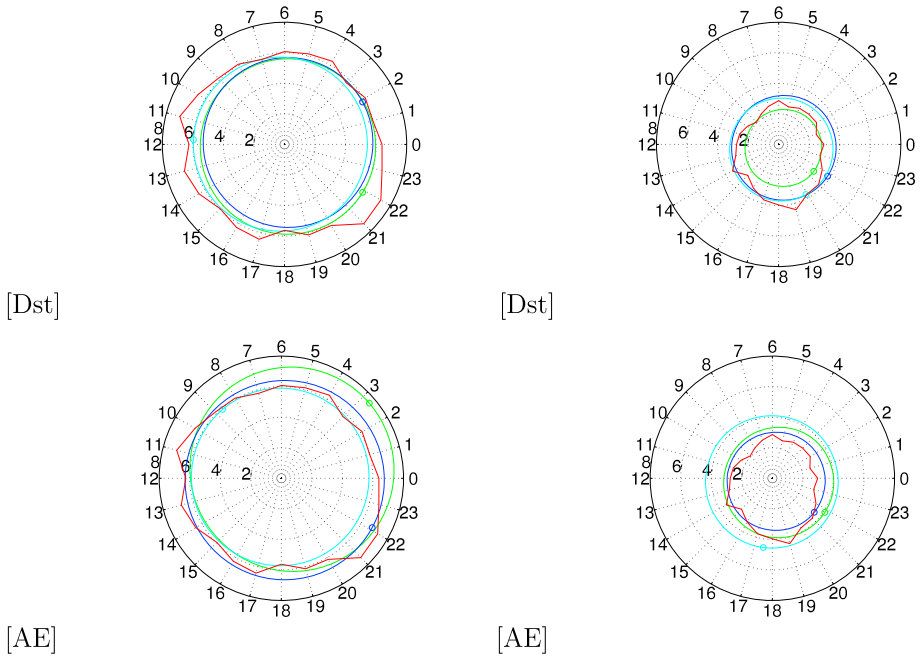


**Figure 4.** Plasmapause shapes obtained from CRRES1 (green), CRRES2 (dark blue), THEMIS1 (light blue), and THEMIS2 (red) models for two levels of geomagnetic activity: (left column) low and (right column) high. Models based on (top row) *Dst* and (bottom row) *AE* indices are shown. For details see text.

models, the geomagnetic index values are taken as $AE = 80$ nT and $Dst = -2$ nT at low geomagnetic activity and $AE = 1200$ nT and $Dst = -250$ nT at high geomagnetic activity. Plasmapause from THEMIS2 model is derived by setting the inputs at low geomagnetic activity to mean $AE = 30$ nT, mean $Kp = 1$, mean $AL = -20$ nT, maximum $AU = 15$ nT, and maximum $SYM\text{-}H = -20$ nT. For high geomagnetic activity the parameters are taken as mean $AE = 800$ nT, mean $Kp = 4$, mean $AL = -560$ nT, maximum $AU = 400$ nT, maximum $SYM\text{-}H = -260$ nT. Here it is important to note that these values used to obtain model predictions cannot be the same for our CRRES2 models because the peak values of the geomagnetic index or SW parameter are generally higher than the one obtained at the highest-correlation time lag [see *Verbanac et al.*, 2015, Tables 2 and 5]. For CRRES2 we set $AE = 2$ nT and $Dst = 30$ nT at low geomagnetic activity; $AE = 700$ nT and $Dst = -70$ nT at high geomagnetic activity. Furthermore, for the CRRES2 Lpp indicators we use here the logarithmic scale in order to make CRRES2 model comparable with other mentioned models. In Figure 4 plasmapause shapes obtained from CRRES1, CRRES2, THEMIS1, and THEMIS2 models are directly compared. At low geomagnetic activity, CRRES1, CRRES2, and THEMIS2 models give the bulge in the night side, from 21 MLT to 03 MLT depending on the used geomagnetic index. In contrast, the THEMIS1 models place the bulge on the day side. However, note that the plasmapause from CRRES1, CRRES2, and THEMIS1 is relatively circular with the difference between its maximum and minimum extension only about 0.5 $R_E$. Only CRRES1 *AE*-based model give a bulge comparable to THEMIS2 model, with difference between the lowest and the largest $L_{pp}$ of around 2 $R_E$. At higher geomagnetic activity, all models give the bulge between 18 MLT and 21 MLT. The difference between the minimum and maximum $L_{pp}$ extension is somewhat larger than at low activity and is again more pronounced for THEMIS2 model (amounting for ~2.5 $R_E$) than for other three models. Generally, THEMIS2 model provides the largest plasmapause variations. This model is built by multi-index fitting using the largest number of plasmapause crossings. On the other side, CRRES1, THEMIS1, and CRRES2 models are obtained by including a first harmonic in MLT providing more smoothed plasmapause shapes. The plasmapause extension within each model (CRRES1, CRRES2, and THEMIS1) is different for *AE* and *Dst* at both levels of geomagnetic activity. In general, *AE* models give somewhat larger plasmapause than *Dst* models. We note that these differences between *AE* and *Dst* models are lower for our CRRES2 model. The RMSE values of CRRES1, CRRES2, THEMIS1, and THEMIS2 models are similar, approximately in the range 0.5–1 L. THEMIS2 has the lowest RMSE in postmidnight and dawnside [see *Liu et al.*, 2015, Figure 6]. All these models have the largest RMSE in duskside and nightside.

**Table 7.** The MLT of Plasmapause Peak at Low and High Geomagnetic Activity Derived From Various Models (See Text for Details)[a]

| Model | Cluster (2007–2011) | CRRES1 (1990–1991) | CRRES2 (1990–1991) | THEMIS1 (2010–2011) | THEMIS2 (2009–2013) | Kwon2015 (THEMIS) (2008–2009) | Katus2015 (IMAGE) (2000–2002) |
|---|---|---|---|---|---|---|---|
| Low | 07–16 | 22–03 | 22–00 | 09–12 | 21 | 20–21 | - |
| High | 16–01 | 20–22 | 21 | 18–20 | 19 | - | around dusk |

[a]The examined year periods are indicated for each model.

Discontinuous models obtained from Cluster-based plasmapause presented in PaperI (thereafter Cluster model), suggest the bulge location on the day side (between 7 MLT and 16 MLT) at low geomagnetic activity, opposite to what we have observed in the present study. On the other side, the observed $L_{pp}$ peak on the premidnight side during more active geomagnetic periods is in accordance with Cluster results. Our RMSE range of values coincides with those from Cluster model. Further comparison with results presented by both *Kwon et al.* [2015] and *Katus et al.* [2015] shows that the plasmapause peak locations derived from our models are consistent with their observations. The first study showed quiet time plasmapause location derived from medians and means of two years (2008 and 2009) of THEMIS-based plasmapause crossings and indicates nearly circular plasmapause with slight bulge in postdusk sector (around 20–22 MLT). This bulge rotates toward dusk under moderate geomagnetic conditions. In the latter study, IMAGE EUV-based plasmapause that results from 43 geomagnetic storms (2000–2002) indicates the bulge position near dusk and across dayside. The MLT of the bulge formation is found to be dependent on the type of solar wind driver. The MLT of the plasmapause peak at low and high geomagnetic activity (characterized with parameter values as listed above) obtained from all above studies are summarized in Table 7.

Finally, we compare the obtained delays in the plasmapause response to the arrival of $L_{pp}$ indicators with those obtained from Cluster model in MLT sectors and also when all MLT are taken together (see Table 3 in Paper I), and those derived by *Larsen et al.* [2007] from IMAGE EUV plasmapause crossings in 2001 (therefore IMAGE2001 models). Note that IMAGE2001 models provide only the delays of the $L_{pp}$ averaged in MLT. Delay times resulting from our models are generally lower than those obtained based on Cluster data set (see Table 3 in Paper I). The delay times derived from all $L_{pp}$ are around 4 h, significantly lower than the Cluster ones which are around 20 h depending on the indicator. Note, however, that these delays are close to the values obtained from IMAGE2001 model. For both CRRES2 and Cluster models, the time lags increase from postmidnight across dayside to midnight. The correlations between $L_{pp}$ and $L_{pp}$ indicators when all MLTs are taken together are, in general, similar for these three models and are between ~0.4 and 0.5.

## 5. Discussion

In the following we list the obtained results and summarize the comparison with other studies. Our main results are as follows:

1. The quality of developed linear models based on both geomagnetic indices and solar wind coupling functions are very similar, although for solar wind parameters less data were available. The only exception is *Ap* model with somewhat larger RMS errors in all sectors and also when all MLTs are considered.
2. The quality of developed continuous MLT models are very similar to the quality of the simple linear models. This shows that with adequate data coverage, the simple models can well simulate the plasmapause shape. Only when all local times are considered, the RMSE are reduced compared to that of simpler models.
3. Simple GI models indicate that plasmapause bulge is likely formed between 18 MLT and 00 MLT at quiet times. Solar wind-based models cannot resolve whether the bulge is between 18 MLT and 00 MLT or between 00 MLT and 06 MLT. At high geomagnetic activity, all models indicate maximum plasmapause extension on the postdusk/premidnight side.
4. Developed continuous models place a plasmapause bulge at low geomagnetic activity between 22 MLT and 00 MLT, depending on the model. All these models predict a bulge around 21 MLT for higher geomagnetic activity.
5. The values of the derived delay times of $L_{pp}$ to the arrival of $L_{pp}$ indicators range from 1 to 18 h, depending on the MLT and on the indicator. For all $L_{PP}$ indicators, the time lag corresponding to the highest correlation is a function of MLT. Lags increase from postmidnight side through dawn to the evening side.

Since different types of $L_{pp}$ indicators (solar wind parameters and geomagnetic indices) provide the same conclusions, we consider our results reliable. As in many previous studies, all of our models show that the plasmapause is closer to the Earth during enhanced geomagnetic activity. The simulated plasmapause shapes are in agreement with past studies for higher level of geomagnetic activity. The differences are found in the comparison with THEMIS1 and Cluster models which both indicate the bulge in the dayside at low geomagnetic activity. However, important to note is that as geomagnetic activity decreases, the plasmapause becomes more circular, and thus, the bulge is less pronounced. Nevertheless, it would be worth to investigate these differences further, e.g., modeling the $L_{pp}$ data set used to build the THEMIS2 model by including the first harmonic in MLT. This may help to distinguish the influences of the applied method and of the number of used data on the results. When new Cluster data will be available, we will perform the analyses to check whether the plasmapause will peak at different MLTs or not at low activity. Generally, the observed discrepancy in the plasmapause shape, as well as in the overall change of the plasmapause radial position likely results from different plasmapause observations, different methodology, unequal number of plasmapause crossings and different parameters used in these studies.

## 6. Conclusion

In this study we analyze the relationship between different $L_{pp}$ indicators based on both solar wind and geomagnetic indices, and CRRES-based plasmapause positions. We built linear fit models for two different data binning (in three and four MLT sectors), and more complex models by including a first harmonic in MLT.

The plasmapause shapes based on all investigated parameters are similar, ensuring that final conclusions are reliable. Monte Carlo bootstrap calculations indicate that *Dst* provides superior models in the dayside. The maximal plasmapause extension is observed in the postdusk side at high geomagnetic activity, confirming findings from previous works. The decrease in the convection electric field places the bulge toward midnight, plasmapause moves away from the Earth and becomes nearly circular. The MLT peak of the plasmapause at low activity should be investigated further, as indicated in the previous section.

The advantage of our approach based on the $L_{pp}$ indicator values at the highest-correlation time lags is that it allows to obtain both the MLT plasmapause distribution and the time offset of the plasmapause response to various $L_{pp}$ indicators. With a clear evidence that the time lags corresponding to the highest correlation is a function of MLT, this study verifies the findings presented in Paper I and contributes to constrain the physical mechanism by which the plasmapause is formed. We propose the following simple scenario of the plasmapause formation. Information about $L_{PP}$ indicators during 30 h before the $L_{PP}$ response reside within the plasmasphere. After 1–4 h (depending on the indicator), plasmasphere responds in the postmidnight MLT sector, where the formation of the new plasmapause is initiated by the interchange instability. Via mechanism of interchange instability motion proposed by *Lemaire and Pierrard* [2008] and *Pierrard et al.* [2008] the interchange instability propagates to other MLT sectors. In such a way, new plasmapause is formed in all MLTs. The follow-up study dedicated to detailed investigation of the above proposed scenario by employing different data set is in progress.

The calculated time lags further indicate that after the plasmapause is formed, information is then quickly passed from postmidnight through dawn to noon (likely at higher rate than the corotation velocity), and then at somewhat slower rate to midnight. The different time delays obtained from CRRES2, IMAGE2001, and Cluster models indicate that the interchange instability by which the plasmapause is formed propagates faster during solar maximum than around solar minimum in the solar activity cycle. This may be associated with the different state of the heliosphere during the studied periods. Namely, both CRESS- and IMAGE-based $L_{pp}$ cover solar maximum only, while Cluster $L_{pp}$ data set embraces declining phase, minimum, and early ascending phase of the solar cycle. This issue should be investigated further and is left for future study.

**Acknowledgments**
Geomagnetic indices *Ap*, *Dst*, and *AE* are obtained from ftp://ftp.ngdc.noaa.gov/STP/GEOMAGNETIC_DATA/INDICES/KP_AP and http://wdc.kugi.kyoto-u.ac.jp/dstae/index.html. The solar wind data are downloaded from OMNIWeb: http://omniweb.gsfc.nasa.gov/form/dx1.html. The CRRES plasmapause database is available upon request from M.B. Moldwin. V. Pierrard thanks the Scientific Federal Policy for the funding in the framework of the program Interuniversity Attraction Pole for the project P7/08 CHARM. M.B. Moldwin was partially financed by NSF AGS1450512.

## References

Brice, N. M. (1967), Bulk motion of the magnetosphere, *J. Geophys. Res.*, *72*, 5193–5211.

Carpenter, D. L., and R. R. Anderson (1992), An ISEE/whistler model of equatorial electron density in the magnetosphere, *J. Geophys. Res.*, *97*(A2), 1097–1108.

Cho, J., D.-Y. Lee, J.-H. Kim, D.-K. Shin, K.-C. Kim, and D. Turner (2015), New model fit functions of the plasmapause location determined using THEMIS observations during the ascending phase of Solar Cycle 24, *J. Geophys. Res. Space Physics*, *120*, 2877–2889, doi:10.1002/2015JA021030.

Darrouzet, F., V. Pierrard, S. Benck, G. Lointier, J. Cabrera, K. Borremans, N. Yu Ganushkina, and J. De Keyser (2013), Links between the plasmapause and the radiation belt boundaries as observed by the instruments CIS, RAPID, and WHISPER onboard Cluster, *J. Geophys. Res. Space Physics*, *118*, 4176–4188, doi:10.1002/jgra.50239.

Heilig, B., and H. Lühr (2013), New plasmapause model derived from champ field-aligned current signatures, *Ann. Geophys.*, *31*(3), 529–539, doi:10.5194/angeo-31-529-2013.

Horne, R. B., and R. M. Thorne (1998), Potential waves for relativistic electron scattering and stochastic acceleration during magnetic storms, *Geophys. Res. Lett.*, *25*, 3011–3014, doi:10.1029/98GL01002.

Katus, R. M., D. L. Gallagher, M. W. Liemohn, A. M. Keesee, and L. K. Sarno-Smith (2015), Statistical storm time examination of MLT-dependent plasmapause location derived from IMAGE EUV, *J. Geophys. Res. Space Physics*, *120*, 5545–5559, doi:10.1002/2015JA021225.

Kozyra, J. U., C. E. Rasmussen, R. H. Miller, and E. Villalon (1995), Interaction of ring current and radiation belt protons with ducted plasmaspheric hiss. 2. Time evolution of the distribution function, *J. Geophys. Res.*, *100*, 21,911–21,920, doi:10.1029/95JA01556.

Kwon, H. J., K. H. Kim, G. Jee, J. S. Park, H. Jin, and Y. Nishimura (2015), Plasmapause location under quiet geomagnetic conditions (Kp less than 1): THEMIS observations, *Geophys. Res. Lett.*, *42*, 7303–7310, doi:10.1002/2015GL066090.

Larsen, B. A., D. M. Klumpar, and C. Gurgiolo (2007), Correlation between plasmapause position and solar wind parameters, *J. Atmos. Sol. Terr. Phys.*, *69*, 334–340, doi:10.1016/jastp.2006.06.017.

Lemaire, J., and V. Pierrard (2008), Comparison between two theoretical mechanisms for the formation of the plasmapause and relevant observations, *Geomagn. and Aeron.*, *48*(5), 553–570, doi:10.1134/S0016793208050010.

Lemaire, J. F., and K. I. Gringauz (1998), *The Earth's Plasmasphere*, Cambridge Univ. Press, New York.

Liu, X., and W. Liu (2014), A new plasmapause location model based on THEMIS observations, *Sci. China Earth Sci.*, *57*, 2552–2557.

Liu, X., W. Liu, J. B. Cao, H. S. Fu, J. Yu, and X. Li (2015), Dynamic plasmapause model based on THEMIS measurements, *J. Geophys. Res. Space Physics*, *120*, 10,543–10,556, doi:10.1002/2015JA021801.

Lorentzen, K. R., J. B. Blake, U. S. Inan, and J. Bortnik (2001), Observations of relativistic electron microbursts in association with VLF chorus, *J. Geophys. Res*, *106*, 6017–6028, doi:10.1029/2000JA003018.

Moldwin, M. B., L. Downward, H. K. Rassoul, R. Amin, and R. R. Anderson (2002), A new model of the location of the plasmapause: CRRES results, *J. Geophys. Res.*, *107*(A11), 1339, doi:10.1029/2001JA009211.

Newell, P. T., T. Sotirelis, K. Liou, C.-I. Meng, and F. J. Rich (2007), A nearly universal solar wind-magnetosphere coupling function inferred from 10 magnetospheric state variables, *J. Geophys. Res.*, *112*, A01216, doi:10.1029/2006JA012015.

Nishida, A. (1966), Formation of plasmapause, or magnetospheric plasma knee, by the combined action of magnetospheric convection and plasma escape from the tail, *J. Geophys. Res.*, *71*, 5669–5679.

O'Brien, T. P., and M. B. Moldwin (2003), Empirical plasmapause models from magnetic indices, *Geophys. Res. Lett.*, *30*(4), 1152, doi:10.1029/2002GL016007.

Pierrard, V., and J. Lemaire (2004), Development of shoulders and plumes in the frame of the interchange instability mechanism for plasmapause formation, *Geophys. Res. Lett.*, *31*, L05809, doi:10.1029/2003GL018919.

Pierrard, V., G. V. Khazanov, J. Cabrera, and J. Lemaire (2008), Influence of the convection electric field models on predicted plasmapause positions during magnetic storms, *J. Geophys. Res.*, *113*, A08212, doi:10.1029/2007JA012612.

Takahashi, K., and B. J. Anderson (1992), Distribution of ULF energy ($f < 80$ mHz) in the inner magnetosphere: A statistical analysis of AMPTE CCE magnetic field data, *J. Geophys. Res*, *97*, 10,751–10,773, doi:10.1029/92JA00328.

Verbanac, G., B. Vršnak, S. Živković, T. Hojsak, A. Veronig, and M. Temmer (2011), Solar wind high-speed streams and related geomagnetic activity in declining phase of solar cycle 23, *Astron. Astrophys.*, *533*, A49, doi:10.1051/0004-6361/201116615.

Verbanac, G., S. Živković, B. Vršnak, M. Bandić, and T. Hojsak (2013), Comparison of geoeffectiveness of coronal mass ejections and corotating interaction regions, *Astron. Astrophys.*, *558*, A85, doi:10.1051/0004-6361/201220417.

Verbanac, G., V. Pierrard, M. Bandic, F. Darrouzet, J.-L. Rauch, and P. Décréau (2015), Relationship between plasmapause, solar wind and geomagnetic activity between 2007 and 2011, *Ann. Geophys.*, *33*, 1271–1283.

## Erratum

In the originally published version of this article, the sixth paragraph of section 2 contained extra information about each sector that could be confusing to the reader. The extraneous information has been removed, and this may be considered the version of record.

In section 2, the sixth paragraph, ": night" has been removed after "Sector1"; ": day" has been removed after "Sector2"; and ": evening" has been removed after "Sector3."